Supported palladium nanoparticles on hybrid mesoporous silica: Structure/activity-relationship in the aerobic alcohol oxidation using supercritical carbon dioxide

Zhenshan Hou [a], Nils Theyssen [a], Axel Brinkmann [a], Konstantin V. Klementiev [b,c], Wolfgang Grünert [b], Michael Bühl [a], Wolfgang Schmidt [a], Bernd Spliethoff [a], Bernd Tesche [a], Claudia Weidenthaler [a], Walter Leitner [a,d,*]

[a] Max-Planck-Institut für Kohlenforschung, Kaiser-Wilhelm-Platz 1, D-45470 Mülheim an der Ruhr, Germany
[b] Lehrstuhl für Technische Chemie, Ruhr-Universität Bochum, Universitätsstr. 150, 44801 Bochum, Germany
[c] Hasylab at DESY, D-22607 Hamburg, Germany
[d] Institut für Technische und Makromolekulare Chemie, Lehrstuhl für Technische Chemie und Petrolchemie, RWTH Aachen, Worringerweg 1, D-52064 Aachen, Germany

ARTICLE INFO

ABSTRACT

The preparation, characterization, and catalytic properties of Pd nanoparticles supported on mesoporous organic–inorganic hybrid materials are described for continuous-flow aerobic oxidation of alcohols using supercritical carbon dioxide ($scCO_2$) as a mobile phase. The nanoparticles were generated "bottom-up" from molecular precursors that were precoordinated to the support through suitable anchor units. The most active material allows high single-pass conversions in $scCO_2$ at temperatures as low as 60°C. This high activity may be associated with the presence of small primary crystallites (approx. 2 nm) that conglomerate to ensembles about 25 nm in size, leading to a larger number of high-indexed planes in small volume units. These findings may provide useful guidelines for further catalyst design on the nanoscale for green oxidation methods.

© 2008 Elsevier Inc. All rights reserved.

1. Introduction

The selective oxidation of alcohols to the corresponding aldehydes or ketones is an important transformation for organic synthesis on laboratory and industrial scales [1–3]. Transition metal-catalyzed oxidations using molecular oxygen have been investigated intensively as green alternatives to replace the more traditional stoichiometric procedures, which generate large amounts of waste and require inefficient purification procedures [4–7]. In particular, palladium-based systems in the form of supported heterogeneous catalysts, nanoparticles, and molecular palladium complexes have been developed for aerobic alcohol oxidation and found to convert various alcohols effectively and selectively to the corresponding aldehydes and ketones [8–25]. In principle, the use of supercritical carbon dioxide ($scCO_2$, $T_c = 31.0°C$, $p_c = 7.4$ MPa) [26–29] allows the implementation of such oxidations in a quasi-solvent-free continuous-flow mode at temperatures far below the boiling points of the organic substrates and products [30–39]. At

the same time, $scCO_2$ provides a safe reaction environment with excellent mass and heat transport properties for aerobic oxidations [40].

Recently, we have developed an efficient system for continuous-flow aerobic alcohol oxidation using palladium nanoclusters that were stabilized and immobilized in a liquid poly(ethylenglycol) (PEG) matrix in combination with supercritical carbon dioxide ($scCO_2$) as the mobile phase [30]. This approach has the potential to solve some of the problems typically associated with homogeneously dispersed nanoparticles, such as deactivation by formation of Pd-black and difficulties in catalyst separation and recycling. However, a stable well-defined Pd-nanoscale catalyst based on a solid and mainly inorganic matrix seems to be even more desirable, because it would allow the use of a simple and highly efficient fixed-bed technology and thereby preclude any risk of depletion or oxidative degradation of the matrix [32,41,42].

Herein we report that organic–inorganic hybrid materials, based on mesoporous silica as a support and 2,2′-dipyridylamine as a linker, allow the efficient immobilization and stabilization of palladium nanoparticles of defined size and aggregation for catalytic aerobic alcohol oxidation using $scCO_2$ as a reaction medium under batchwise and continuous-flow, fixed-bed conditions (Fig. 1). Recently, similar materials have been developed for applications in conventional solvents [42–44]. In addition to the development of
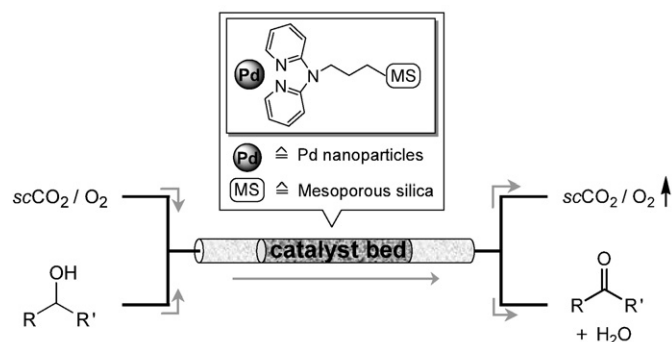
Fig. 1. Schematic drawing of the general reaction concept.

a quasi-solvent-free continuous-flow process, the present study includes a detailed analysis of the supported nanoscale particles. The combined results indicate that the chosen reduction method of the Pd(II) precursor (benzyl alcohol vs hydrogen) exerts a controlling effect on the texture and oxidation state distribution of the obtained palladium species, resulting in very significant differences in the catalytic activity.

2. Experimental

2.1. Synthesis of materials

All organic solvents used in this work were dried by standard procedures. All of the syntheses were performed under argon. ^{1}H NMR and ^{13}C NMR spectra were recorded on a Bruker DPX 300 instrument. Pd(OAc)$_2$, 5% Pd/C, and Pd%/Al$_2$O$_3$ were obtained from Aldrich and used as received.

2.1.1. Synthesis of 1

Commercially available 2,2′-dipyridylamine (1.0 g, 5.84 mmol) was dissolved in 15 mL of dry THF. This solution was added to a suspension of NaH (0.14 g, 5.85 mmol) in 50 mL of dry THF. The mixture was stirred under argon at 0 °C for 1 h and then added to a solution of 3-iodopropyltriethoxysilane (synthesized from 3-chloropropyltriethoxysilane; 1.95 g, 5.92 mmol) in 10 mL of dry THF. The resulting reaction mixture was stirred at room temperature under argon for 16 h. The solvent was evaporated under high vacuum at 35 °C, and the resulting residue was taken up again in toluene (100 mL). After filtration of the salts and washing with toluene (3 × 10 mL), the filtrate was concentrated under vacuum, resulting in a yellow oil (1.71 g, 4.52 mmol, 76.5%). ^{1}H NMR (δ, 300 MHz, CDCl$_3$): 0.48–0.53 ppm (m, 2H, CH_2Si), 1.63–1.85 ppm (m, 2H, CH_2), 3.68 ppm (q, 6H, OCH_2), 1.06 ppm (t, 9H, CH$_2$$CH_3$), 3.96 ppm (t, 2H, N$CH_2$), 6.51–8.24 ppm (m, 8H, Ar H). ^{13}C NMR (δ, 75 MHz, CDCl$_3$): 6.34 ppm (CH$_2$$Si$), 23.9 ppm ($CH_2$), 49.84 ppm ($CH_2$N), 57.78 ppm (O$CH_2$), 18.18 ppm (CH$_2$$CH_3$), 113.0 (Ar), 117.14 (Ar), 138.60 (Ar), 148.76 (Ar), 156.01 (Ar). MS (EI): $m/z = 376$ [M + H$^+$], 163 [Si(OC$_2$H$_5$)$_3^+$]. Elemental analysis: Calculation for C$_{19}$H$_{29}$N$_3$O$_3$Si: C: 60.77, H: 7.78, N: 11.19, O: 12.78, Si: 7.48; Found: C: 60.44; H: 7.65, N: 10.88, Si: 7.36.

2.1.2. Synthesis of 2

The hybrid material was synthesized by co-hydrolysis and polycondensation of mixtures **1** and tetraethylorthosilicate (TEOS) in the presence of n-hexadecylamine as a template. The molar composition of the mixture was 0.88 TEOS:0.12 **1**:0.28 n-hexadecyl-amine:29.6 H$_2$O:9.1 ethanol. The xerogel was prepared as described previously [45]. The reaction mixture was stirred for 24 h. The resulting solid was filtered and washed with ethanol. Surfactant was removed from the product by Soxhlet extraction with

ethanol for 20 h. Before use, the extract was dried under vacuum at 80 °C for 14 h.

2.1.3. Synthesis of 3

To a Schlenk-tube filled with 2.5 g of **2**, 0.65 g of Pd(OAc)$_2$ and 100 mL of dry acetone were added and stirred for 24 h. The resulting suspension was filtered and washed with acetone and dichloromethane, then dried at 80 °C for 14 h. The resulting product was a yellow powder.

2.1.4. Synthesis of 4

First, 2 g of **3** was conditioned for 17 h by refluxing it in a 50-mL mixture of toluene and benzyl alcohol (80:20, V/V). The resulting solid was then washed completely with toluene and acetone, and then dried at 80 °C for 12 h to obtain a dark-green powder. Elemental analysis: 2.22% N and 7.02% Pd.

2.1.5. Synthesis of 5

First, 0.7 g of **3** was loaded into an autoclave, then reduced for 4 h at 40 bar H$_2$ and 110 °C. After reduction, the hydrogen was released slowly from the autoclave, resulting in a brown powder.

2.2. Characterization of the synthesized materials by XRD, BET area, TEM, ^{29}Si MAS NMR, XPS, and XAFS

The powder X-ray diffraction (XRD) patterns for qualitative phase analysis were collected on a Stoe STADI P transmission diffractometer in transmission geometry with a primary monochromator curved germanium (111) and a linear position sensitive detector, with Cu$K_{\alpha 1}$: 1.54060 Å as a radiation source. The data were collected in the range of 0–10° 2θ with a step width of 0.01° 2θ. For the measurements, the sample was prepared between two polyacetate foils.

Nitrogen sorption isotherms were measured at 77 K with a Quantachrome Instruments Nova 3000e sorption analyzer. Before the measurements, the samples were evacuated at 393 K for 8 h. Transmission electron microscopy (TEM) and energy-dispersive X-ray analysis (EDX) were used to investigate structural features of the catalysts with a Hitachi HF-2000 instrument. ^{29}Si MAS NMR spectroscopy was recorded on a Bruker Avance 500WB instrument using a 4-mm MAS probe at a spinning rate of 10 kHz, 30 s recycle delay, 2800 scans, and 2.2 μs $\pi/4$ pulse.

XPS measurements were performed with a Kratos HSi spectrometer with a hemispherical analyzer and a monochromatized Al$K\alpha$ X-ray source ($E = 1486.6$ eV), operated at 15 kV and 15 mA. For the narrow scans, an analyzer pass energy of 40 eV was applied. The hybrid mode was used as lens mode. The base pressure in the analysis chamber was 6×10^{-10} Torr. To account for charging effects, all spectra are referred to Si 2p at 103.45 eV.

XAFS measurements were carried out at the X1 station of HASYLAB (DESY, Hamburg, Germany) using a double-crystal Si(311) monochromator. The energy resolution was estimated from the angular beam size as 7.1 eV (standard deviation) at the Pd K-edge. Samples were pressed into discs of suitable thickness in a glove box, and the discs were sealed air-tight in Kapton tape before being inserted into the XAFS experiment. The spectra were recorded in transmission mode at low temperature ($T = 80$ K) to decrease the Debye–Waller factors, and a Pd foil was measured simultaneously (between the second and third ionization chambers) for energy calibration purposes. Details of the analysis procedure are given in the ESI section.

Table 1
Key structural and analytical parameters for **2–5**, together with catalytic data

	2	3	4	5
Reduction	–	None	Benzyl alcohol	Hydrogen
Color	Colorless	Yellow	Greenish	Brown
BET ($m^2\,g^{-1}$)[a]	990	699	688	677
Pore size (nm)[a]	3.5	n.d.	2.6	n.d.
Pd-content (wt%)	–	7.12	7.01	7.06
N-content (wt%)	2.43	2.32	2.22	2.18
Oxidation state of bulk Pd (XAFS)	–	Pd(II) (ca. 100%)	Pd(0)/Pd(II), (33%:67%)	Pd(0)/Pd(II), (29%:71%)
Oxidation state of surface Pd (XPS)	–	Pd(II) (ca. 100%)	Pd(0)/Pd(II), (55%:45%)	Pd(0)/Pd(II) (84%:16%)
Single pass conversion of **6a**[b]	–	3%	41%	9%
TON (turnover number)	–	60	800	180
Selectivity for **7a**[b]	–	98.7%	98.2%	98.6%

[a] For details of the sorption measurement see Supporting information; n.d. = not determined.
[b] Average values over 28 h on stream, cf. Fig. 6.

2.3. Typical procedure for the alcohol oxidation with functionalized hybrid catalysts under supercritical carbon dioxide

Safety warning: The use of compressed gases and especially O_2 in the presence of organic substrates requires appropriate safety precautions and must be carried out using suitable equipment.

Batchwise catalytic oxidation of alcohol in $scCO_2$: 75 mg of catalyst **4** and 2.50 mmol alcohol (n(substrate)/n(Pd) = 50) was placed in a 36 mL stainless-steel high-pressure reactor. The reactor was pressured with a defined CO_2/O_2 mixture (19.5 g, $c(O_2)$ = 8 vol%) and heated under vigorous stirring to the desired temperature for a specified time (see Table 1). The total pressure was 18 MPa. After reaction, CO_2 was released slowly through two −35 °C serial cold traps. The products were collected by washing the cold traps and the autoclave with diethyl ether. The combined fractions were then analyzed by ^{1}H NMR and GC.

Continuous-flow, fixed-bed catalytic oxidation of alcohol in $scCO_2$: The reactions were performed in a fixed-bed stainless steel tubular reactor with an inner diameter of 7.5 mm and 20 mL volume (see Fig. 1). The temperature of the catalyst bed was controlled by a pumped thermal oil fluid, which kept the reactor at 60 °C. Pure quartz (80 mesh, 3.5 g) was used to dilute the catalyst bed (0.2 g catalyst). A glass bead was placed above the catalyst bed to ensure an optimal distribution of reactants at the beginning of the catalyst bed. A prewarmed (50 °C) continuous stream of CO_2/O_2 was passed through the tubular reactor at a flow rate of approximately 7.5 $l\,h^{-1}$ (exit flow at ambient conditions; total pressure, 15 MPa). The substrate was fed into the CO_2 stream before it entered the reactor with a HPLC pump at a rate of 1.0 mL h^{-1}. The reaction mixture was isolated in two sequential cold traps at −35 °C from the exit flow on depressurization of the supercritical solvent. The cold traps was replaced periodically after about 2 h, and their combined content was analyzed by ^{1}H NMR and GC. Details on the experimental setup are given in the Supporting information (Fig. 5S).

3. Results and discussion

### 3.1. Catalyst preparation and characterization

In previous studies, Pd nanoparticles have been generated on inorganic supports by impregnation (on, e.g., TiO_2 [25], hydroxyapatite [16], or active carbon [46] and by chemical vapor deposition [47], or encapsulation/decomposition [48,49]) on MCM-41. We followed a different technique, starting from molecular precursors that were incorporated through organofunctional groups in the inorganic framework during preparation of the mesoporous material (one-pot method; Scheme 1) [42,50–53]. The trialkoxylsilyl derivative of 2,2′-dipyridylamine **1** was used as a coordinative linker for the Pd-precursor. (See Supporting information for details of

the preparation.) The hydrolysis/condensation of **1** with tetraethylorthosilicate (TEOS) in the presence of *n*-hexadecylamine led to the functionalized mesoporous material **2**. After the template was removed by extraction with ethanol, the product was treated with an acetone solution of palladium acetate to give the silica bound coordination compound **3** (Pd loading, 7.1%). Finally, the material was reduced either with benzylic alcohol under reflux conditions or with molecular hydrogen to yield the Pd-containing mesoporous silica materials **4** and **5**, respectively (Scheme 1). The preparation methods led to distinct materials with high reproducibility as demonstrated by the excellent concordance of the XAFS spectra of independent synthesized and measured samples (see Supporting information).

Table 1 presents information on the texture, composition, oxidation state, and catalytic properties of the synthesized materials. The XRD pattern of the colorless hybrid material **2** shows a single diffraction peak corresponding to a d-spacing of 4.1 nm. The N_2 isotherms indicate a BET area of 990 $m^2\,g^{-1}$ and confirm the mesoporous structure with pore diameters around 3.5 nm [54–63]. These measurements, together with HRTEM micrographs of the material, clearly indicate a wormhole pore structure. From the ^{29}Si MAS NMR spectra, the resonances near −100 and −110 ppm represent the Q^3 HOSi(OSi)$_3$ and Q^4 Si(SiO)$_4$ environments of the SiO$_4$, whereas the signals around −66 ppm arise from T^3 connectivities of the organic-functionalized silicon centers (see Supporting information for details).

The structure of the mesoporous material **2** remained largely unperturbed on incorporation of the Pd centers, but BET area and pore sizes became somewhat smaller compared with the organic functionalized hybrid materials, as expected. The XRD patterns showed no visible reflections at higher angles, indicating the absence of long-range ordering. Differences in the Pd-containing materials **3–5** were macroscopically indicated by their different colors. The silica-bound coordination compound **3** was bright yellow, whereas **5** was a brown powder. Material **4** appeared greenish, somewhere between the two other solids.

XPS analysis demonstrated that **3** contained exclusively Pd(II) centers, as expected; however, two distinct signals indicated the presence of two surface-bound species (Fig. 2a). Adsorbed [Pd(OAc)$_2$]$_3$, or PdO, can be excluded as sources for these signals, because no corresponding intensities were found in the EXAFS spectra (Fig. 3b). The signal at lower binding energy (336.9 eV, 37 at%) can be assigned to a Pd environment with two oxygen and two nitrogen ligands. The other signal (338.4 eV, 63 at%) most likely resulted from a pure oxidic environment. These data are most consistent with the formation of a trinuclear cluster [(AcO)$_2$Pd(μ-AcO)$_2$Pd(μ-AcO)$_2$Pd(N–N)–silica] as the main species (theoretical: Pd[O]$_4$: 66%, Pd[O]$_2$[N]$_2$: 33%) on the surface, likely together with small amounts of a mononuclear coordination compound of type [(AcO)$_2$Pd(N–N)–silica]. These assignments are in
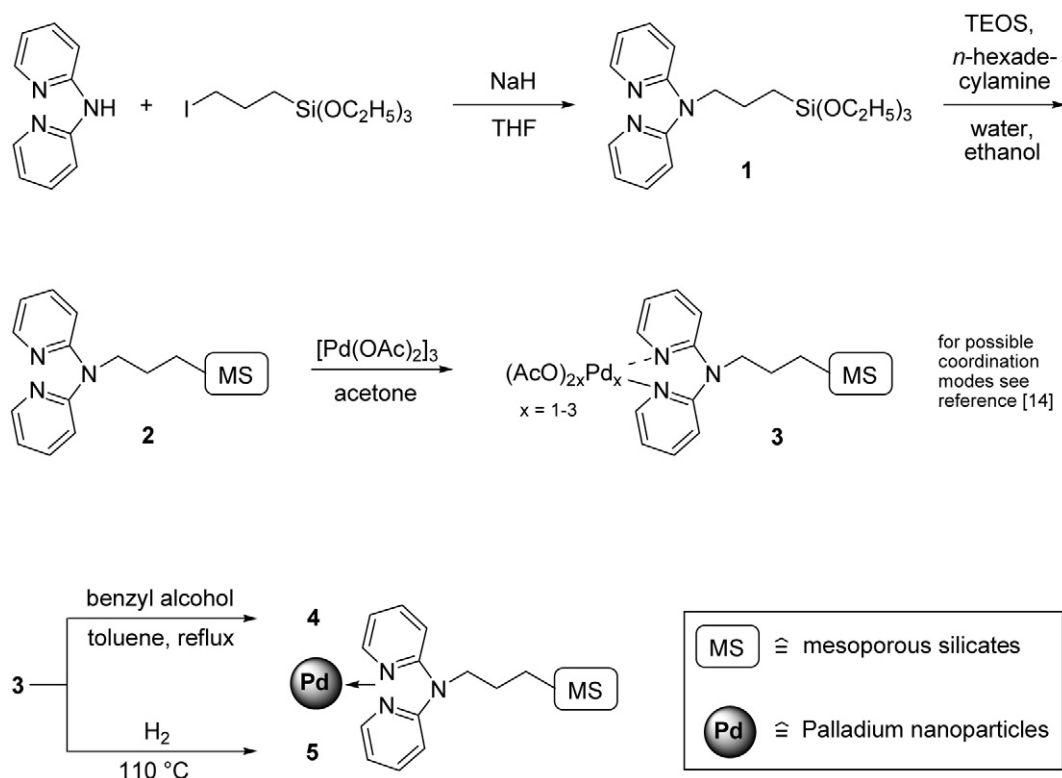
Scheme 1. Synthesis of functionalized organic–inorganic hybrid materials **4** and **5** containing Pd-nanoparticles on mesoporous silica.
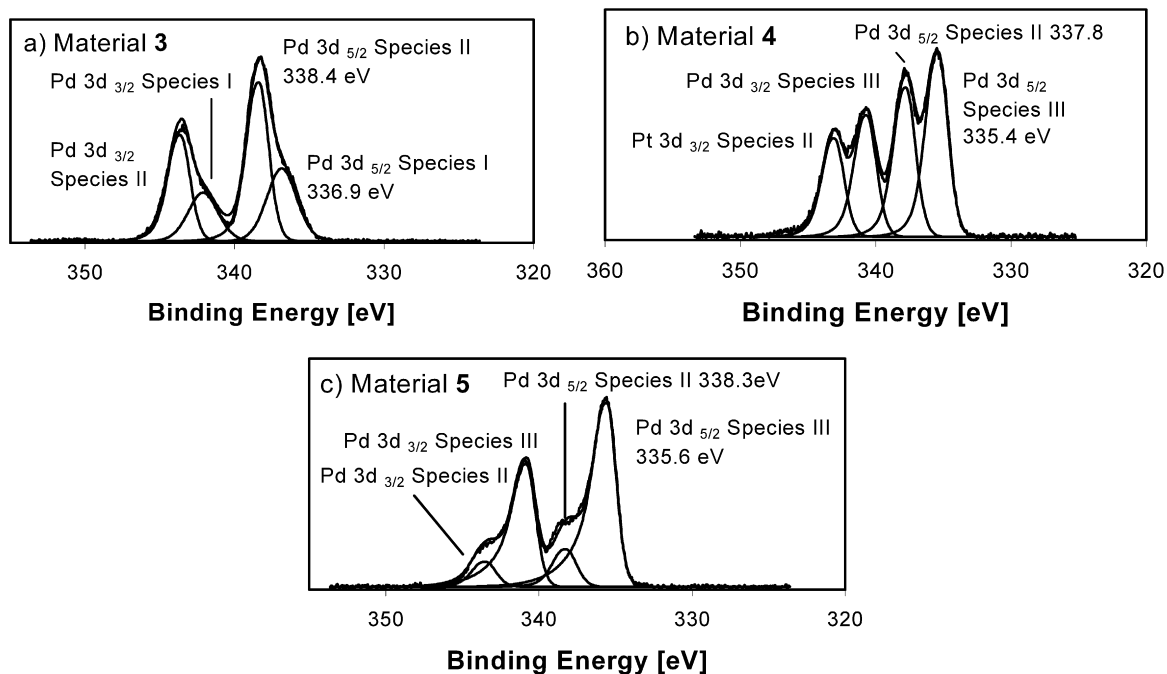

Fig. 2. XPS analysis (Pd 3d spectra) for the surface-bound Pd-centers in materials **3** (a), **4** (b), and **5** (c). Species I and II are assigned to Pd(II) centers, whereas species III results from Pd(0). See text for details.

line with calculated charges on Pd for appropriate model compounds [64]. Based on the ratio of linker:Pd from elemental analysis, it may be concluded that ca. 55% of the linker remained noncoordinated.

The XPS spectra of the material **5** indicate that the Pd(II) centers were reduced to a great extent by hydrogen treatment, resulting in 84% of Pd(0)-centers at the surface (Fig. 2c). In contrast, ma-

terial **4** contained significant amounts of unreduced palladium sites corresponding to 45% Pd(II) (337.8 eV) and 55% Pd(0) (335.4 eV) at the surface (Fig. 2b). Thus, hydrogen treatment appeared to be more efficient for the reduction of surface-bound Pd-centers than benzyl alcohol reduction. To obtain information on the metal particles not only at the surface, but also throughout the bulk material, we performed a XAFS study to assess the overall oxidation state of
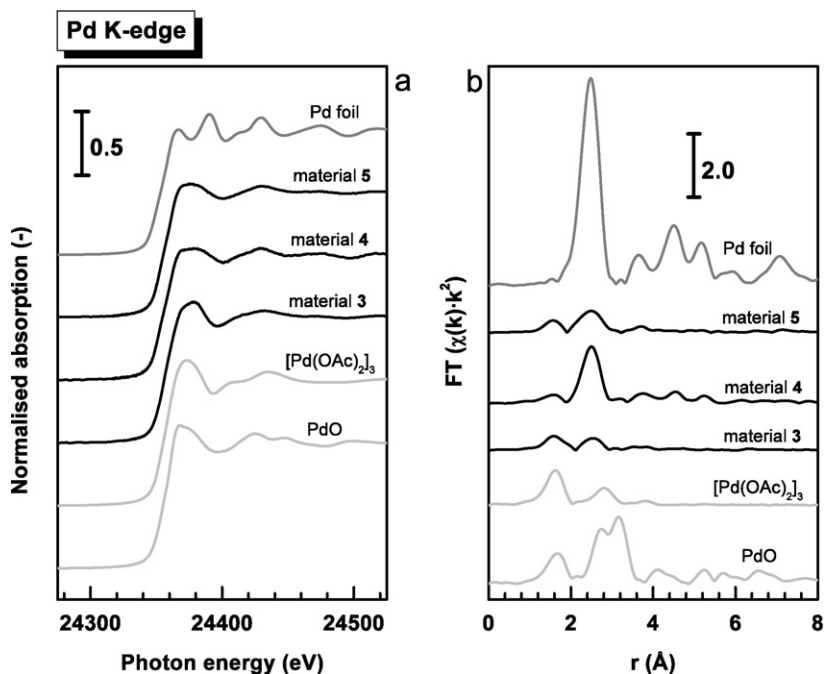
Fig. 3. XAFS spectra of material **3–5** and reference compounds Pd foil, PdO and Pd acetate. (a) XANES, (b) EXAFS (Fourier transformation of k^2-weighted spectra).

Pd and to gain insight into the local environment of the particles inside the mesopores of the materials **3–5**.

Fig. 3 shows XANES spectra together with the Fourier-transformed EXAFS for materials **3–5** together with Pd-containing reference materials. In full accordance with the XPS data, the features of material **3** are clearly distinct from PdO. A precise analysis of the spectra from $[Pd(OAc)_2]_3$ also revealed explicit differences, indicating that the presence of significant amounts of $[Pd(OAc)_2]_3$ was highly unlikely. Overall, the data are fully consistent with the trinuclear coordination mode $[(AcO)_2Pd(\mu\text{-}AcO)_2Pd(\mu\text{-}AcO)_2Pd(N\text{–}N)\text{–silica}]$ derived from the XPS data.

After reduction with benzyl alcohol, a signal for the first Pd–Pd coordination sphere in metallic palladium was clearly visible in the EXAFS spectrum (albeit with very small amplitude), along with a signal for the residual coordination of Pd with a light element (ca. 1.6 Å, uncorrected) in material **4**. Target transformation analysis of the XANES region revealed the presence of two components, identified as precursor **3** and Pd nanoparticles, the data for which were obtained from an independent study on Pd/C catalysts [65–67]. These (carbon-supported) Pd nanoparticles exhibited a Pd–Pd coordination number of 8.0 ± 0.6, corresponding to a particle diameter of 1.0–1.5 nm as derived from a geometrical correlation between coordination number and (spherical) particle size [68]. The linear fit of the XANES region (Fig. 4) yielded a composition corresponding to 32.6% of Pd in nanoparticles and 67.4% in unconverted precursor **3**, which directly corresponds to the degree of reduction of the bulk material. Using this same ratio, we could closely reproduce the EXAFS spectra by superimposing the spectra measured with **3** and with the Pd nanoparticles [66,67] (Fig. 4), suggesting that these were the only significant Pd phases present in material **4**.

Comparing the data from XPS and the analysis of the XAFS measurements reveals that the palladium in the bulk of material **4** was reduced significantly less than the surface-exposed centers (cf. Table 2). This difference was even more pronounced in material **5**, obtained from hydrogen reduction, for which XPS indicated a reduction degree of 84%. The EXAFS spectrum of **5** showed considerable resemblance to that of precursor **3**, but with significant differences in the XANES region (Fig. 3). Analyzing the data in

a similar manner as for material **4** (see Supporting information) resulted in Pd compositions of 70.7% in unconverted precursor **3** and 29.3% in Pd nanoparticles, significantly smaller than those required for the best fit with material **4** (nanoparticles in material **5**: coordination number–6.6 ± 0.6, diameter–0.7–1.1 nm). It should be noted that the attempt to reproduce the EXAFS spectrum as a linear combination of the component spectra resulted in a less satisfactory agreement in material **5**, indicating that the sample may contain another, highly dispersed Pd(0) phase.

These XAFS measurement results indicate incomplete reduction for the bulk material in both cases, but also suggest the presence of significantly larger particles with partially metallic character in material **4**. A combination of TEM and EDX analysis provided further insight into the nature of the two materials in terms of nanoparticle fraction. In material **4**, large nanoparticulate units were observed, consisting of primary crystallites with an average size of 2.4 nm (in fair agreement with the 1.5 nm obtained from XAFS) that aggregate into conglomerates with typical diameters of about 25 nm (Fig. 5A, a–c). Due to the restricted inner width of the mesoporous channels (about 4 nm), it is obvious that these ensembles are present exclusively at the external surfaces. No such large secondary particles were found in material **5**, obtained by hydrogen reduction. Most of the particles at the external surface appeared to be primary particles, with an average diameter of 6.5 nm (Fig. 5B, a–c). This value is almost an order of magnitude larger than that derived from XAFS data, further supporting the conclusion that **5** contained an additional Pd(0) phase of much higher dispersion that was not visible on TEM.

3.2. Catalytic performance

To assess the catalytic performance of the new hybrid materials **3–5**, we evaluated then in the aerobic alcohol oxidation of benzyl alcohol (**6a**) to give benzaldehyde (**7a**) using supercritical carbon dioxide ($scCO_2$) as the mobile phase under continuous-flow conditions similar to those developed for PEG-stabilized Pd_{561} clusters (Scheme 2; Fig. 1; see Supporting information for details) [30, 32]. Due to $scCO_2$'s unique combination of gas-like mixing and liquid-like solvent properties, a homogeneous feed of CO_2, O_2, and
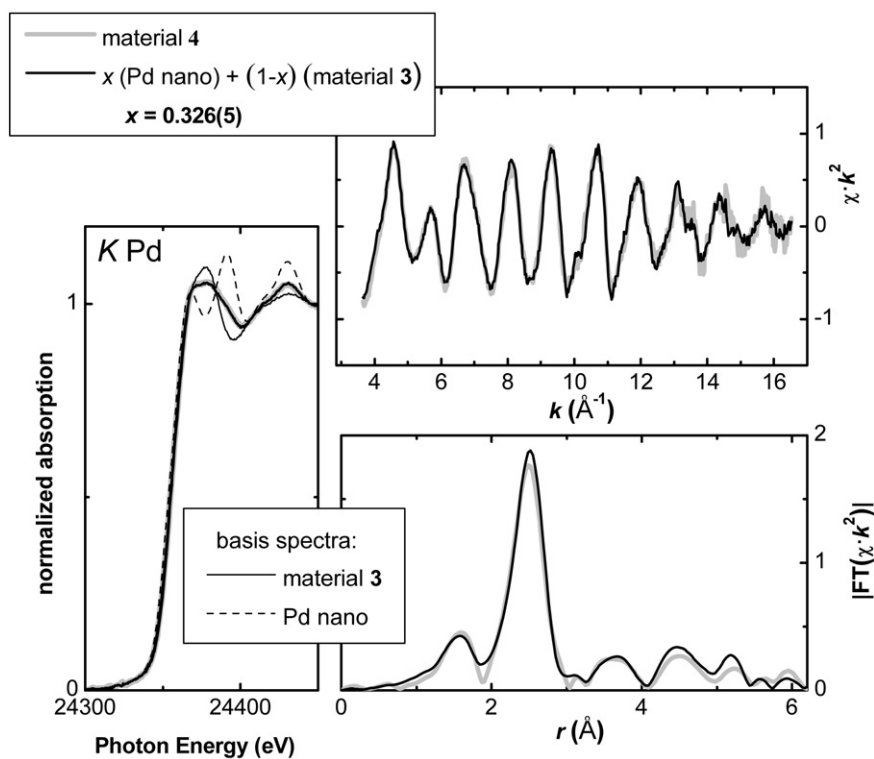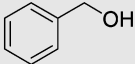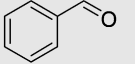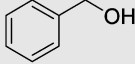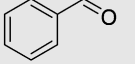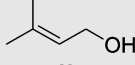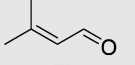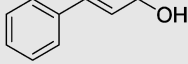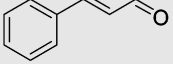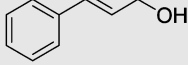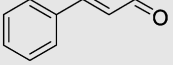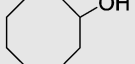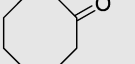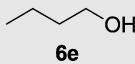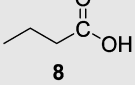
Fig. 4. XANES fit for material **4** and the resulting EXAFS.

Table 2
Aerobic oxidation of alcohols **6a–e** catalyzed by **4** in scCO$_2$[a]

Entry	Substrate	Product	T (°C)	t (h)	Conversion (%)	Selectivity (%)
1	**6a**	**7a**	60	12	92.5	98.4
2	**6a**	**7a**	80	5	99.5	89.8
3	**6b**	**7b**	80	7	97.8	96.4
4	**6c**	**7c**	60	8	98.5	99.6
5	**6c**	**7c**	80	4	99.2	92.6
6	**6d**	**7d**	80	18	92.6	98.7
7	**6e**	**8**	80	8	11.5[b]	93.0[c]

[a] General reaction conditions: m(catalyst **4**) = 75 mg, n(substrate) = 1.65 mmol, d(CO$_2$/O$_2$) = 0.52 g mL^{-1}, c(O$_2$) = 8 vol%.
[b] Yield **8** = 5.5%, yield butyl butyrate = 5.2%, yield butanal = 0.8%.
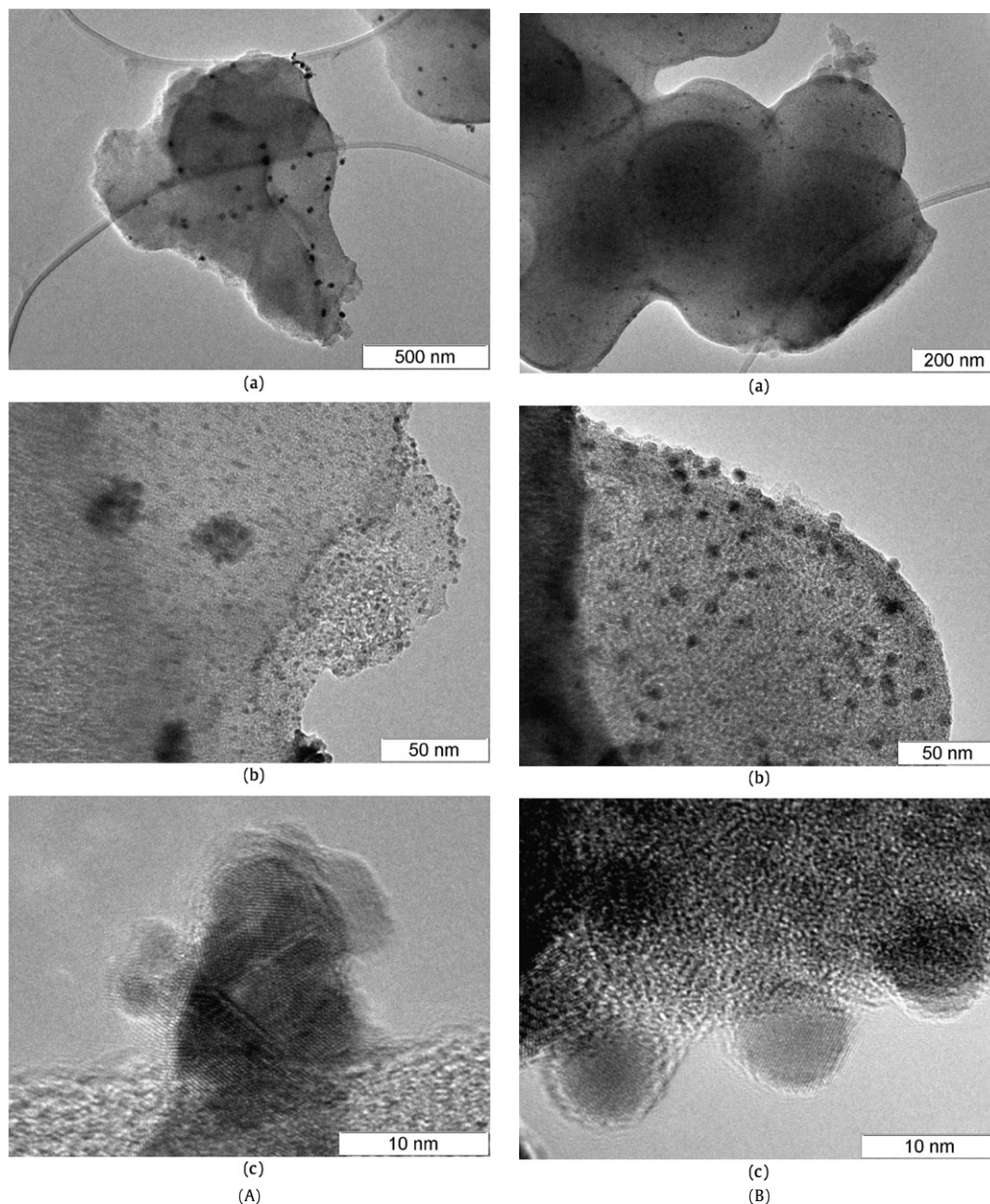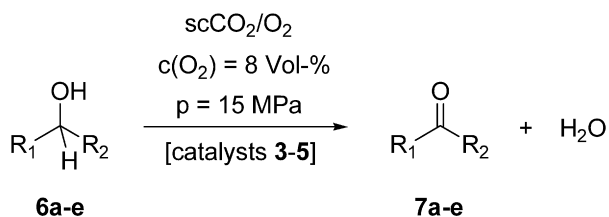[c] Selectivity towards **8** and its butyl ester.

Fig. 5. (A) TEM micrographs of material **4** before using it as a catalyst in the alcohol oxidation reaction. The magnification increases from (a) to (c). (B) TEM micrographs of material **5** before using it as a catalyst in the alcohol oxidation reaction. The magnification increases from (a) to (c).

Scheme 2. Aerobic alcohol oxidation with Pd-based mesoporous catalysts **3–5** under supercritical conditions. For definition of **6a–e/7a–e** and other products see Table 2.

6a–e/7a–e can be transported in a gas-like manner through the catalyst bed at temperatures far below the boiling point of the substrate and products [26–30,32–37]. Furthermore, $scCO_2$ has been found to enhance the rate of mass transfer inside the channel of porous materials [69,70]. This behavior can facilitate rapid removal

of products, avoiding the formation of overoxidized side products. In addition, a low operation temperature would be expected to increase the lifetime of the catalyst material, avoiding deactivation processes. However, all of these beneficial properties can be exploited only with the proper choice of catalyst material.

Fixed-bed columns were prepared from the catalyst materials mixed homogeneously with quartz for better mechanical stability (catalyst:quartz ratio = 17.5:1). Short paths of glass were used to seal the beds on either side of the column. The rest of the setup was identical to that described previously [30,32]. Such parameters as O_2/substrate/CO_2 ratio, system pressure, and flow rate were fixed at standard conditions to benchmark the performance of the various catalyst materials. The temperature was set at 60 °C, because preliminary screening indicated significant activity for material **4** already at that value. This temperature is considerably lower
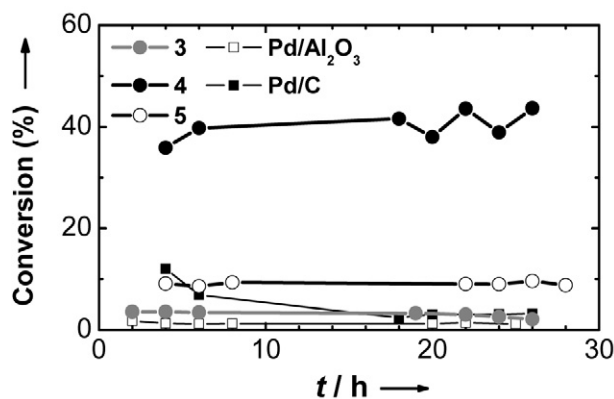
Fig. 6. Continuous-flow fixed-bed aerobic oxidation of benzyl alcohol (**6a**) in scCO$_2$ with different catalysts; m(catalyst) = 0.20 g, T = 60 °C, p(CO$_2$/O$_2$: 92/8) = 15 MPa, flow rate = 1 mL h^{-1}, exit flow (normal pressure) = 7.5 L h^{-1}.
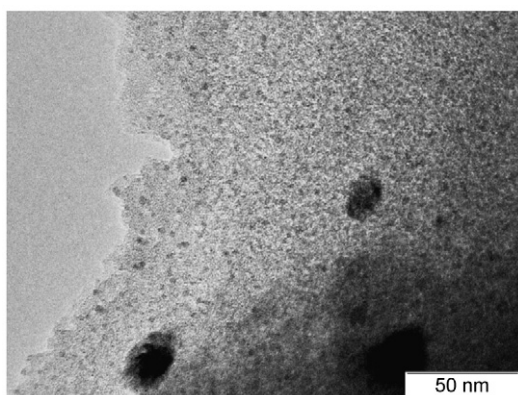

Fig. 7. TEM micrograph of material **4** after using it as a catalyst in the oxidation of **6a** (after 24 h on stream).

than that used with previous catalysts, which generally require $T \geqslant 80$ °C, in most cases $\geqslant 100$ °C.

As Fig. 6 shows, the commercial Pd/Al$_2$O$_3$ gave only negligible single-pass conversion for benzyl alcohol **6a** as a prototypical substrate at 60 °C under scCO$_2$ continuous-flow conditions. Pd/C gave an initially significant conversion of around 12%, which rapidly dropped to <5%. A similar marginal conversion was observed with the heterogenized Pd(II) complex in material **3**. Material **5**, obtained by hydrogen reduction, exhibited significant and stable conversion around 9%. Finally, catalyst **4** showed a more than four-fold greater activity and excellent stability in scCO$_2$ under mild conditions. On average, single-pass conversions of 41% and selectivities of >98% for **7a** were achieved at temperatures as low as 60 °C and remained constant over more than 28 h on stream. Under the nonoptimized continuous-flow conditions used in the present study, these data correspond to a space-time yield of >100 g **7a** per liter of reactor volume per hour. Based on the actual catalyst material, the productivity corresponds to 2.1 g of **7a** per g of **4** per hour (TON after 26 h = 800; TOF = 31 h^{-1} based on the total amount of Pd).

TEM micrographs obtained for samples of material **4** recovered from the reactor after 24 h on stream showed no indication of significant further agglomeration of the Pd particles during the catalytic process (compare Fig. 5A and Fig. 7). Furthermore, the level of palladium in the colorless product was <1 ppm. These data suggest negligible particle growth through Ostwald ripening and metal leaching under these conditions. Clearly, the low-temperature activity of the catalyst system, which allows operation of the continuous process at 60 °C, was beneficial in this respect. For example, increasing the reaction temperature with **7a** to 80 °C led to an

increase in single-pass conversion to 65%, but palladium was detected at around 5 ppm in the slightly yellow product, and the selectivity was reduced to 90%.

To assess the possible scope of the continuous alcohol oxidation in scCO$_2$, catalyst **4** was evaluated in batchwise experiments using structurally different alcohols **6a–e** (Table 2). In the temperature range of 60–80 °C, benzylic (**6a**), allylic (**6b–c**), and cyclic aliphatic (**6d**) alcohols were converted in high yields into the corresponding carbonyl compounds within similar reaction times (entries 1–6), indicating that comparable space-time yields could be achieved under continuous-flow conditions. Operating at 60 °C generally gave somewhat higher selectivity, especially in the presence of other potentially oxidizable groups (entries 1/2 and 4/5). In general, the reactions could be carried out at lower temperatures or reduced reaction times compared with earlier systems based on PEG-supported Pd$_{561}$ clusters [30,32]. At the same time, the overoxidation of primary alkanols, such as 1-butanol (**6e**), which led to the corresponding acid (**8**) in free form and in form of the corresponding butyl ester, was largely suppressed with catalyst **4**.

4. Conclusion

Here we have shown that the immobilization of palladium nanoclusters on organic/inorganic hybrid mesoporous silicates led to highly active catalysts for aerobic alcohol oxidation in scCO$_2$ under batchwise and continuous-flow, fixed-bed conditions. The combination of a highly active solid catalyst material with scCO$_2$ as a mobile phase allowed a reaction engineering setup resembling a typical gas-phase process at temperatures far below the boiling point of the substrates and products. Together with the nature of the support, this is believed to contribute to the catalysts' high stability by preventing particle growth and metal leaching.

Application of this strategy requires a catalyst material of sufficiently high activity. In this respect, the performance of material **4** seems very promising. Most notably, **4** showed significantly higher activity than material **5**, which is identical in terms of porous structure, Pd loading, and bulk oxidation state. Detailed analysis of the materials revealed two major differences that may be related to the different activities. First, material **4** contained more unreduced Pd(II) centers at the surface. However, no evidence for an interaction between the Pd(0) and Pd(II) centers was obtained in this study, and the isolated Pd(II) centers were found to be largely inactive in material **3** and in physical mixtures of **3** and **5** under the present conditions [33,37,71,72]. Second, there was a significant difference in the nature of the Pd(0) phases present in the two materials [9]. The hydrogen reduction used for the preparation of material **5** yielded medium-sized (approx. 6 nm) primary particles of very regular shape together with a second, highly dispersed Pd(0) phase. Although this provided many accessible surface Pd centers, it apparently was not the ideal situation for high activity [73]. In contrast, the alcoholic reduction method for sample **4** resulted in a texture containing small primary crystallites (ca. 2 nm) that conglomerated to larger units of about 25 nm. Because of the many different crystalline orientations in such ensembles, many high-indexed planes are present in small volume units. The resulting high number of accessible edges and corners provide many potential sites for catalytically active Pd(0)-centers, giving a plausible explanation for the high activity of material **4** [74,75].

The findings of the present study emphasize once again that the application of unconventional reaction media, such as supercritical CO$_2$, must be integrated with the development and molecular understanding of suitable catalysts to exploit the potential benefits offered by these advanced fluids. In the present study, the reduction method used in nanoparticle preparation has a critical influence on the size and agglomeration of the primary crystallites, which in turn define the catalytic performance of the ma-

terials. Interestingly, the data suggest that there is an optimum balance between high surface area and surface defects, and thus that nanoscale agglomerates can exhibit significantly higher activities compared with isolated small primary particles in highly dispersed phases. This may be a useful guideline for further catalyst design on the nanoscale for green oxidation methods.

Acknowledgments

Supporting information

Further analytical characterizations using XRD, N_2 sorption experiments, ^{29}Si MAS NMR spectroscopy and XAFS, and a schematic presentation of the continuous-flow setup. This material is available free of charge at http://www.sciencedirect.com.

Please visit DOI: 10.1016/j.jcat.2008.07.002.

References

[1] R.A. Sheldon, I.W.C.E. Arends, G.-J.T. Brink, A. Dijksman, Acc. Chem. Res. 35 (2002) 774.
[2] R.A. Sheldon, J.K. Kochi, Metal-Catalyzed Oxidation of Organic Compounds, Academic Press, New York, 1981, p. 350.
[3] B.M. Trost, I. Fleming, S.V. Ley, Comprehensive Organic Synthesis, Pergamon, Oxford, 1991.
[4] M.J. Schultz, M.S. Sigman, Tetrahedron 62 (2006) 8227.
[5] P.T. Anastas, J.C. Warner, Green Chemistry: Theory and Practice, Oxford University Press, Oxford, 1998.
[6] P.T. Anastas, M. Kirchhoff, Acc. Chem. Res. 35 (2002) 686.
[7] P.T. Anastas, R.L. Lankey, Green Chem. 2 (2000) 289.
[8] J. Muzart, Tetrahedron 59 (2003) 5789.
[9] B.-Z. Zhan, A. Thompson, Tetrahedron 60 (2004) 2917.
[10] B.A. Steinhoff, I.A. Guzei, S.S. Stahl, J. Am. Chem. Soc. 126 (2004) 11268.
[11] S. Shimazu, T. Uehara, A. Asami, T. Hara, N. Ichikuni, J. Mol. Catal. A: Chem. 282 (2008) 28.
[12] H.L. Wu, Q.H. Zhang, Y. Wang, Adv. Synth. Catal. 347 (2005) 1356.
[13] A. Corma, H. Garcia, A. Leyva, J. Mol. Catal. A: Chem. 230 (2005) 97.
[14] M.S. Kwon, N. Kim, C.M. Park, J.S. Lee, K.Y. Kang, J. Park, Org. Lett. 7 (2005) 1077.
[15] T. Mallat, A. Baiker, Chem. Rev. 104 (2004) 3037.
[16] K. Mori, T. Hara, T. Mizugaki, K. Ebitani, K. Kaneda, J. Am. Chem. Soc. 126 (2004) 10657.
[17] T. Iwasawa, M. Tokunaga, Y. Obora, Y. Tsuji, J. Am. Chem. Soc. 126 (2004) 6554.
[18] S. Paavola, K. Zetterberg, T. Privalov, I. Csöregh, C. Moberg, Adv. Synth. Catal. 346 (2004) 237.
[19] T. Nishimura, S. Uemura, Synlett (2004) 201.
[20] U.R. Pillai, E. Sahle-Demessie, Green Chem. 6 (2004) 161.
[21] Y. Uozumi, R. Nakao, Angew. Chem. Int. Ed. 42 (2003) 194.
[22] G.-J.T.I. Brink, W.C.E. Arends, M. Hoogenraad, G. Vespui, R.A. Sheldon, Adv. Synth. Catal. 345 (2003) 497.
[23] D.R. Jensen, M.J. Schultz, J.A. Mueller, M.S. Sigman, Angew. Chem. Int. Ed. 42 (2003) 3810.
[24] G. Kovtun, T. Kameneva, S.L. Hladyi, M. Starchevsky, Y. Pazdersky, I. Stoarov, M. Vargaftik, I. Moiseev, Adv. Synth. Catal. 344 (2002) 957.
[25] K. Ebitani, Y. Fujie, K. Keneda, Langmuir 15 (1999) 3557.
[26] P.G. Jessop, W. Leitner (Eds.), Chemical Synthesis Using Supercritical Fluids, Wiley–VCH, Weinheim, 1999.
[27] A. Baiker, Chem. Rev. 99 (1999) 453.
[28] P. Licence, J. Ke, M. Sokolova, S.K. Ross, M. Poliakoff, Green Chem. 5 (2003) 99.
[29] W. Leitner, Acc. Chem. Res. 35 (2002) 746.
[30] M. Caravati, J.-D. Grunwaldt, A. Baiker, Catal. Today 126 (2007) 27.
[31] Z. Hou, N. Theyssen, A. Brinkmann, W. Leitner, Angew. Chem. Int. Ed. 44 (2005) 1346.
[32] Z. Hou, N. Theyssen, W. Leitner, Green Chem. 9 (2007) 127.
[33] J.-D. Grunwaldt, M. Caravati, A. Baiker, J. Phys. Chem. B 110 (2006) 9916.
[34] M. Caravati, D.M. Meier, J.-D. Grunwaldt, A. Baiker, J. Catal. 240 (2006) 126.
[35] M. Caravati, J.-D. Grunwaldt, A. Baiker, Phys. Chem. Chem. Phys. 7 (2005) 278.
[36] M. Caravati, J.-D. Grunwaldt, A. Baiker, Catal. Today 91–92 (2004) 1.
[37] J.-D. Grunwaldt, M. Caratati, M. Ramin, A. Baiker, Catal. Lett. 90 (2003) 221.
[38] S. Campestrini, M. Carraro, R. Ciriminna, M. Pagliaro, U. Tonellato, Adv. Synth. Catal. 347 (2005) 825.
[39] R. Ciriminna, S. Campestrini, M. Pagliaro, Org. Biomol. Chem. 4 (2006) 2637.
[40] N. Theyssen, Z. Hou, W. Leitner, Chem. Eur. J. 12 (2006) 3401, and references therein.
[41] B. Karimi, A. Zamani, J.H. Clark, Organometallics 24 (2005) 4695.
[42] B. Karimi, S. Abedi, J.H. Clark, V. Budarin, Angew. Chem. Int. Ed. 45 (2006) 4776.
[43] C. Li, Q. Zhang, Y. Wang, H. Wan, Catal. Lett. 120 (2008) 126.
[44] S.F.J. Hackett, R.M. Brydson, M.H. Gass, I. Harvey, A.D. Newman, K. Wilson, A.F. Lee, Angew. Chem. Int. Ed. 46 (2007) 8593.
[45] P.T. Tanev, T.J. Pinnavaia, Chem. Mater. 8 (1996) 2068.
[46] H. Bönnemann, G. Braun, W. Brijoux, R. Brinkmann, S.A. Tilling, K. Seevogel, K. Siepen, J. Organomet. Chem. 520 (1996) 143.
[47] P. Mehnert, J.Y. Ying, Chem. Commun. (1997) 2215.
[48] M.D. Jones, M.J. Duer, S. Hermans, Y.Z. Khimyak, B.F.G. Johnson, J.M. Thomas, Angew. Chem. Int. Ed. 41 (2002) 4726.
[49] B.F.G. Johnson, Top. Catal. 24 (2003) 147.
[50] M.H. Valkenberg, W.F. Hölderich, Catal. Rev. 44 (2002) 321.
[51] A.P. Wight, M.E. Davis, Chem. Rev. 102 (2002) 3589.
[52] D.E. De Vos, M. Dams, B.F. Sels, P.A. Jacobs, Chem. Rev. 102 (2002) 3615.
[53] G. Kickelbick, Angew. Chem. Int. Ed. 43 (2004) 3102.
[54] Y. Mori, T.J. Pinnavaia, Chem. Mater. 13 (2001) 2173.
[55] W. Zhang, T.R. Pauly, T.J. Pinnavaia, Chem. Mater. 9 (1997) 2491.
[56] P.T. Tanev, T.J. Pinnavaia, Chem. Mater. 8 (1996) 2068.
[57] T.R. Pauly, T.J. Pinnavaia, Chem. Mater. 13 (2001) 987.
[58] C.C. Chen, E.J. McKimmy, T.J. Pinnavaia, K.F. Hayes, Environ. Sci. Technol. 38 (2004) 4758.
[59] Y. Liu, T.J. Pinnavaia, J. Mater. Chem. 14 (2004) 1099.
[60] S.S. Kim, T.R. Pauly, T.J. Pinnavaia, Chem. Commun. (2000) 835.
[61] R.J.P. Corriu, E. Lancelle-Beltran, A. Mehdi, C. Reye, S. Brandes, R. Guilard, J. Mater. Chem. 12 (2002) 1355.
[62] T.J. Pinnavaia, D.B. Jackson, J.E.G. Mdoe, J.H. Clark, New J. Chem. 23 (1999) 539.
[63] R.J.P. Corriu, A. Mehdi, C. Reye, C. Thieuleux, Chem. Mater. 16 (2004) 159.
[64] Density functional calculations (RI-BP86/6-31G* level with Stuttgart–Dresden pseudopotential on Pd) for the charge of the palladium atom with Natural Population Analysis (NPA) give the following results: [Pd(OAc)$_2$]$_3$: +0.80 [(AcO)$_2$-Pd(η^2-dma)] (mononuclear model compound for 3, dma = dipyridylmethylamin): +0.75 [(AcO)$_2$Pd^2(μ_2-OAc)$_2$Pd^1(η^2-dma)] (binuclear model compound for 3): Pd^2 = +0.79, Pd^1 = +0.75 [(AcO)$_2$Pd^3(μ_2-AcO)$_2$Pd^2(μ_2-OAc)$_2$Pd^1(η^2-dma)] (open trinuclear model compound for 3): Pd^3 and Pd^2 = +0.81, Pd^1 = +0.75 [Pd^1(μ_2-OAc)(AcO)Pd^3(μ_2-AcO)$_2$Pd^2(μ_2-OAc)$_2$Pd^1(η^1-dma)] (closed trinuclear model compound for 3): Pd^3 and Pd^2 = +0.81, $\sqrt{Pd}^1$ = +0.78.
[65] It is known that the XANES of small particles differs in amplitude from that of a bulk material. Hence, we performed the linear XANES fitting using not the spectrum of bulk Pd but spectra of Pd nanoparticles from an earlier study of Pd/C catalysts, in which Pd(0) was the only palladium state detected [66]. Attempts to fit the XANES region of material 4 by a sum of the basis spectra of Pd foil, PdO and [Pd(OAc)$_2$]$_3$ resulted in significantly less agreement between measurement and models.
[66] K.V. Klementiev, A.Yu. Stakheev, O.P. Tkachenko, N.N. Tolkachev, W. Grünert, Hasylab Annual Report 2002.
[67] A.Yu. Stakheev, O.P. Tkachenko, G.I. Kapustin, N.S. Telegina, G.N. Baeva, T.R. Brueva, K.V. Klementiev, W. Grünert, L.M. Kustov, Russ. Chem. Bull. 53 (2004) 528.
[68] M. Borovski, J. Phys. IV 7 (1997) 259.
[69] A.I. Cooper, Adv. Mater. 15 (2003) 1049.
[70] P.L. Dhepe, A. Fukuoka, M. Ichikawa, Phys. Chem. Chem. Phys. 5 (2003) 5565.
[71] J.-D. Grunwaldt, M. Caravati, A. Baiker, J. Phys. Chem. B 110 (2006) 25587.
[72] A.F. Lee, S.F.J. Hackett, J.S.J. Hargreaves, K. Wilson, Green Chem. 8 (2006) 549.
[73] F. Li, Q. Zhang, Y. Wang, Appl. Catal. A 334 (2008) 217.
[74] B. Ioan, A. Miyazaki, K.-I. Aika, Appl. Catal. B 59 (2005) 71.
[75] F. Maillard, S. Schreier, M. Hanzlik, E.R. Savinova, S. Weinkauf, U. Stimming, Phys. Chem. Chem. Phys. 7 (2005) 385.